ehp ENVIRONMENTAL HEALTH PERSPECTIVES
http://www.ehponline.org

Using ToxCast™ Data to Reconstruct Dynamic Cell State Trajectories and Estimate Toxicological Points of Departure

Imran Shah, R. Woodrow Setzer, John Jack, Keith A. Houck, Richard S. Judson, Thomas B. Knudsen, Jie Liu, Matthew T. Martin, David M. Reif, Ann M. Richard, Russell S. Thomas, Kevin M. Crofton, David J. Dix, and Robert J. Kavlock

http://dx.doi.org/10.1289/ehp.1409029

Received: 1 August 2014
Accepted: 12 October 2015
Advance Publication: 16 October 2015

Environ Health Perspect DOI: 10.1289/ehp.1409029
Advance Publication: Not Copyedited

Using ToxCast™ Data to Reconstruct Dynamic Cell State Trajectories and Estimate Toxicological Points of Departure

Imran Shah,[1] R. Woodrow Setzer,[1] John Jack,[2] Keith A. Houck,[1] Richard S. Judson,[1] Thomas B. Knudsen,[1] Jie Liu,[3] Matthew T. Martin,[1] David M. Reif,[2] Ann M. Richard,[1] Russell S. Thomas,[1] Kevin M. Crofton,[1] David J. Dix,[1] and Robert J. Kavlock[1]

[1]National Center for Computational Toxicology, Office of Research and Development, U.S. Environmental Protection Agency, Research Triangle Park, North Carolina, USA; [2]Bioinformatics Research Center, North Carolina State University, Raleigh, North Carolina, USA; [3]Oak Ridge Institute for Science Education (ORISE), USA

Address correspondence to Imran Shah, U.S. Environmental Protection Agency, 109 TW Alexander Drive (B205-01), Research Triangle Park, NC 27711 USA. Telephone: (919) 541-1391. E-mail: shah.Imran@epa.gov

Running title: Cell state trajectories and tipping points

Acknowledgment: Cell culture, chemical exposure, and HCI imaging was conducted by Apredica under EPA contract EP-D-13-013.

Disclaimer: The views expressed in this article are those of the authors and do not necessarily represent the views or policies of the U.S. Environmental Protection Agency.

Competing financial interests: The authors declare they have no actual or potential competing financial interests.

Abstract

Background: High-content imaging (HCI) allows simultaneous measurement of multiple cellular phenotypic changes and is an important tool for evaluating the biological activity of chemicals.

Objectives: Our goal was to analyze dynamic cellular changes using HCI to identify the "tipping point" at which the cells did not show recovery towards a normal phenotypic state.

Methods: The effects of 967 chemicals were evaluated using HCI in HepG2 cells over a 72 h exposure period to concentrations ranging from 0.4 to 200 μM. The HCI endpoints included p53, c-Jun, phospho-Histone H2A.x, alpha tubulin, phospho-Histone H3, alpha tubulin, mitochondrial membrane potential, mitochondrial mass, cell cycle arrest, nuclear size and cell number. A computational model was developed to interpret HCI responses as cell-state trajectories.

Results: Analysis of cell-state trajectories showed 336 chemicals produced tipping points, whereas HepG2 cells were resilient to the effects of 334 chemicals up to the highest concentration (200 μM) and duration (72 h) tested. Tipping points were identified as concentration-dependent transitions in system recovery and the corresponding critical concentrations were generally between 5 and 15 times (25th and 75th percentiles, respectively) lower than the concentration that produced any significant effect on HepG2 cells. The remaining 297 chemicals require more data before they can be placed in either of the former categories.

Conclusions: These findings show the utility of HCI data for reconstructing cell state trajectories, and provide insight into adaptation and resilience of *in vitro* cellular systems based on tipping points. Cellular tipping points could be used to define a point of departure for risk-based prioritization of environmental chemicals.

Introduction

A major focus in public health has been to understand and limit potential adverse health effects of chemicals. However, despite an expectation of safety from the general public, tens of thousands of chemicals in commerce have been evaluated on the basis of closely related analogs, but lack chemical-specific toxicity information (Judson et al. 2009). The lack of toxicity information has led to national and international efforts to use *in vitro* high-throughput screening (HTS) methods to collect data on biochemical and cellular responses following chemical treatment *in vitro* (Kavlock et al. 2009; Attene-Ramos et al. 2013). A key element of toxicity testing in the 21st century (NRC 2007; Boekelheide and Andersen 2010) is to conceptually organize HTS data into pathways that when sufficiently perturbed, lead to adverse outcomes. One challenge associated with the new vision has been to assess 'tipping points' beyond which pathway perturbations invoke a lasting change that could ultimately lead to an adverse effect.

The present study is part of the EPA's ToxCast™ project, which aims to develop *in vitro* screens to identify potentially hazardous substances for further targeted testing (Kavlock et al. 2012). We used high-content imaging (HCI) (Giuliano et al. 2006), which applies automated image analysis techniques to capture multiple cytological features using fluorescent labels, and to measure the concentration-dependent dynamic changes in the state of HepG2 cells. Although not fully metabolically capable, HepG2 cells can undergo continuous proliferation in culture and have a demonstrated capacity to predict hepatotoxicity of pharmaceutical compounds with good sensitivity and specificity (O'Brien et al. 2006; Abraham et al. 2008). Using computational tools HCI responses were deconvoluted into cell state trajectories and analyzed by their propensity to recover to normal (basal) conditions over the test period. The critical concentration associated

with non-recoverable cellular trajectories were determined, where possible, and compiled into a novel chemical classification scheme. We discuss how these 'tipping points' in cellular systems function might be used to define a point of departure for risk-based prioritization of environmental chemicals.

Methods

Cell culture

HepG2 cells were obtained from ATCC and used before passage 20. Cells were maintained and expanded in complete media (10% FBS in MEM/EBSS supplemented with Penicillin/Streptomycin, L-glutamine and non-essential amino acids). Cell culture reagents were obtained from VWR International. HepG2 cells were harvested by trypsinization and plated at different densities in 25 µl of culture medium, depending on incubation time, in clear-bottom, 384-well microplates (Falcon #3962) that were coated with rat tail collagen I. The cells were incubated overnight to allow for attachment and spreading.

Chemical treatments

HepG2 cells were treated with 967 chemicals from ToxCast Phase-I and Phase-II libraries (EPA 2014). Cells were treated with DMSO as a solvent control at a final concentration of 0.5% (v/v) or with compounds in DMSO with a resulting final DMSO concentration of 0.5% (v/v). Compound treatment was done at 0.39, 0.78, 1.56, 3.12, 6.24, 12.5, 25, 50, 100 and 200 µM in duplicate on each plate. Cells were treated with ToxCast Phase I compounds for 1, 24, and 72 h and ToxCast Phase II compounds for 24 and 72 h only. Carbonylcyanide m-chlorophenylhydrazone (CCCP) and taxol were used as positive controls for mitochondrial

function and cytoskeletal stability, respectively; DMSO served as the negative control for this experiment.

Cell Staining and Fluorochroming

Cells were fixed by the direct addition of 50 µl formaldehyde in HBSS to a final concentration of 3.7%. After incubation in the fixation medium for 30 min at room temperature, cells were rinsed twice with HBSS and treated with cell permeabilization buffer (16 µL of 0.5% Triton X-100) for 10 min at room temperature before labeling. For mitochondrial membrane potential and mitochondrial measurements, pre-fixed cells were incubated with 50 uL of MitoTracker® Red CMXRos (Invitrogen) at 250 nM for 30 min before fixation. In the remaining cases, post-fixed cells were labeled by incubation with a multiplexed mixture of primary antibodies in HBSS for 60 min at room temperature to detect immunoreactivity of: c-Jun (1:500), phospho-Histone H3 (1:100), phospho-Histone H2A.x (1:200), TP53 (1:400), α-tubulin (1:200) and Hoechst 33342 (2 µg/ml). Cells were labeled for multiplexed imaging on two separate plates: (i) Hoechst 33342, MitoTracker Red, phospho-Histone H3, α-tubulin, and (ii) Hoechst 33342, phospho-Histone H2A.x, c-Jun. A final rinse with HBSS (50 µl) was performed prior to analysis. The primary and secondary antibodies for proteins were: phospho-Histone H3 (Rabbit anti-phospho-histone H3 and FITC-Donkey anti-rabbit IgG), phospho-Histone H2A.x (Mouse anti-phospho-histone H2A.X and FITC-Donkey anti-mouse IgG), c-Jun (Rabbit anti-phospho-c-jun and Cy3-Donkey anti-rabbit IgG), TP53 (Sheep anti-p53 and Cy5-Donkey anti-sheep IgG), α-tubulin (Mouse anti-a-tubulin and Cy5-Donkey anti-mouse IgG). These antibodies are available as the CellCiphr HepG2 assay kit from Millipore.

Image acquisition, analysis and feature extraction

Digital images of each well were captured using a Cellomics ArrayScan VTI (Thermo Scientific Cellomics®) (0.8 NA objective, 0.63x optical coupler, and XF-93 filter set) at 20x magnification. The images were acquired using the autofocus feature of the ArrayScan instrument, which entails the following steps. First, the camera focuses on channel 1 (Hoechst 33342) where nuclei are identified. Second, a Z offset of 1 μm is used for capturing mitochondria (MitoTracker Red). Third, a Z offset of -2 μm is used for capturing the cytoskeleton (tubulin). Six digital images were captured in each well and analyzed using BioApplication software provided with the instrument. All images were analyzed using the Compartmental Analysis and Cell Cycle Analysis BioApplication software from Cellomics. The Cell Cycle BioApplication software (Cellomics 2007a) used the nuclear stain to identify valid cells, to measure nuclear diameter, and to quantify DNA content. These features were used to calculate the average nuclear size, cell cycle arrest (ratio of 2N/4N) and cell number. The Compartmental Analysis BioApplication software (Cellomics 2007b) was used to measure the average cell level intensities for c-Jun phosphorylation, p53 protein activation, phospho-Histone H2A.x activation, mitochondria, and alpha-tubulin. The average intensity of mitochondria was used to define mitochondrial membrane potential while the total intensity was used to define mitochondrial mass. Data from cellular features measured in the nucleus were excluded in wells where there was significant decrease in nuclear size and brightness. Detailed documentation about the algorithms and parameter used by the BioApplication software for this analysis are available upon request. Cellular features were aggregated at the well level to quantify the following endpoints: p53 activation, c-Jun activation (stress kinase), phospho-Histone H2A.x (DNA

damage produced by oxidative stress), phospho-Histone H3 (mitotic arrest), alpha tubulin (microtubules), mitochondrial membrane potential, mitochondrial mass, cell cycle arrest, nuclear size and cell number. Supplemental Material, Table S1 summarizes the relationship between cellular endpoints, stains/fluorochromes, BioApplication software, and the specific algorithms used for extracting cell level features. The raw image data (captured by the ArrayScan VTI) and well level data for all chemical treatment concentrations, time points, and stains/fluorochromes was stored in a custom database, which is freely available (ftp://www.epa.gov/comptox/toxcast-hci-hepg2-a). Representative HCI images captured 1, 24 and 72 h after treatment with CCCP, taxol, butachlor, fludioxonil and fluazinam are shown in Supplemental Material, Figures S1(a), (b), (c), (d) and (e), respectively.

Data processing and normalization

Concentration response data from the HCI experiment were smoothed and normalized for every chemical, endpoint and time. The raw concentration responses were smoothed using a Hamming window (Blackman and Tukey 1958) of length 7. The raw concentration-dependent responses for reference chemicals, CCCP and taxol, are shown in Supplemental Material, Figures S2(a) and S2(b), respectively. The raw time-dependent responses for reference chemicals, CCCP and taxol, are shown in Supplemental Material, Figures S2(c) and S2(d), respectively. Further examples of raw smoothed concentration and time dependent responses for fludioxonil, fluazinam, and butachlor are shown in Supplemental Material, Figure S3. Next, the smoothed data (r) for endpoints measured on each plate were normalized by the median response (r*) to calculate perturbations as the logarithm (base 2) of fold change values. The normalized changes

($x=log_2 r/r^*$) were also standardized ($z = (x - x^*)/\sigma_x$) to evaluate the importance of perturbations (where σ_x is the standard deviation of x). The lowest effect concentration (LEC) for each chemical and endpoint was calculated as the concentration that produced a fold change perturbation at least one standard deviation (i.e., $\sigma_x = 1$) above or below the median value. An absolute perturbation greater than one standard deviation was called a "hit" (i.e., $|\sigma_x| > 1$). The LEC was estimated by numerically solving for: $|z| = 1$ (the minimum value was selected if there were multiple solutions). The efficacy was measured as maximum positive or negative value of x.

System trajectory and dynamics

Each concentration and duration of chemical treatment produced a system perturbation ($\boldsymbol{X}$), which was represented by the vector: $\boldsymbol{X} = [x_{sk}, x_{os}, x_{p53}, x_{mt}, x_{mm}, x_{mmp}, x_{ma}, x_{cca}, x_{ns}, x_{cn}]$ (where the subscripts sk, os, mt, p53, mm, mmp, ns, ma, cca, and cn denote stress kinase, oxidative stress, p53, microtubules, mitochondrial mass, mitochondrial membrane potential, mitotic arrest, cell cycle arrest, nuclear size and cell number, respectively). The vector perturbation was also summarized by a scalar magnitude (X), which was calculated as the Euclidean norm ($X = |\boldsymbol{X}| = (\sum x_i^2)^{1/2}$). We defined a trajectory (T) as the dynamic response of the system to a chemical concentration as a temporal sequence of scalar perturbations, $T = \{X^0, X^1, X^2, .., X^t, .., X^n\}$. The scalar system perturbation was assumed continuous across concentration and time ($X= f(c,t)$) and estimated from experimental data (we assumed that the system was unperturbed at t=0, i.e. $f(c,0) =0$). The velocity of the system (V) was defined as the rate of change of the scalar system perturbation ($V = \partial X/\partial t$) and calculated as the slope of X with respect to time, t. At a given time point, normal, recovering, and non-recovering trajectories are defined by: $V = 0$, $V<0$ and $V>0$,

respectively. The concepts of system trajectory, velocity, and recovery are illustrated in Figures 1(a), (b) and (c), respectively.

Quantifying system recovery across concentrations

We assumed V formed a two-dimensional surface from which the recovery of the system could be analyzed at any time (t) across concentrations (c) (see Figure 1(d)). Consider a hypothetical parabolic relationship between V and c at a fixed time (shown in Figure 1(e)). At low concentrations V is positive, which suggests that the system perturbation is increasing. As the concentration increases, V decreases until it reaches a turning point, and then it begins to increase. These trends can be summarized by rate of change of V with respect to concentration ($\partial_c V = \partial V/\partial c = \partial^2 X/\partial t \partial c$), which can have three possible values: (a) $\partial_c V<0$ for concentrations that produce recovery, (b) $\partial_c V>0$ for concentrations that do not produce recovery, and (c) $\partial_c V=0$ signifies the concentration corresponding to the critical point for system recovery. For each chemical, the empirical relationship between $\partial_c V$ and different treatment concentrations at 72 h was estimated by B-spline interpolation and numerically solved for $\partial_c V=0$ to calculate the critical concentration (denoted as, C_{cr}). After resampling 50 subsets of the concentration-velocity pairs for each chemical, $\partial_c V$ was fitted and solved for $\partial_c V=0$ to construct a distribution, which was used to estimate the 95% confidence interval for C_{cr}. We also recorded the trends in $\partial_c V$ as a function of concentration and the frequency with which the resampled subsets produced critical points (i.e. parabolic trends in $\partial_c V$ with maxima), or produced recovery (i.e. parabolic trends in $\partial_c V$ with minima).

Data analysis software

The data processing, storage, analysis and visualization was conducted using the freely available Python programming language (Python 2014) and associated open source libraries. The software is freely available from authors upon request.

Results

General Characteristics of Cellular Effects

The concentration-response profiles of 967 chemicals were analyzed across the 10 HCI endpoints and three time points to identify hits. Almost half of the chemicals (43.7% or 432/967) produced a hit for at least one of the 10 endpoints by 72 h. Chemical-wise, 13.7% (132/967) changed mitochondrial membrane potential, 15.2% (147/967) altered mitochondrial mass, 22.7% (220/967) invoked oxidative stress, 9.4% (91/967) altered microtubules, 14.1% (137/967) perturbed stress kinase, 27.1% (262/967) altered p53 protein distribution, 17.3% (167/967) produced cell cycle arrest, 26.9% (260/967) invoked mitotic arrest, 7.7% (74/967) changed nuclear size and 32.2% (311/967) decreased cell number. Time-wise, altered mitochondrial membrane potential (29/308) and p53 activity (14/308) were the two most frequent perturbations at 1 h (only Phase-I compounds (EPA 2014) were tested at 1 h); perturbations in p53 activity (168/967), mitotic arrest (157/967), and cell loss (155/967) were the most frequent effects at 24 h. Finally, decrease in cell number (303/967), mitotic arrest (249/967) and p53 activity (228/967) were the most frequent effects at 72 h. The LEC for all 967 chemicals across the 10 endpoints are provided as Supplemental Material, Excel Table S1.

Cellular perturbations

Interpreting the results of the HCI experiment proved to be a complex problem because nearly half of the chemicals produced hits across multiple endpoints at different times. The dynamic perturbations produced by a representative subset of chemicals are shown in Figure 2 (data for all chemicals is provided as Supplemental Material, Excel Table S2). Each row of heatmaps displays the perturbations produced by increasing concentrations (only 0.39, 1.56, 6.25, 25, and 100 μM treatments are shown) of six chemicals: (a) octanoic acid, (b) dimethyl terephthalate, (c) chlorpyrifos-methyl, (d) butachlor, (e) dicofol, and (f) oxadiazon. Each heatmap shows perturbations (colors), times (rows) and endpoints (columns). For example, the row of heatmaps in Figure 2(a) shows the perturbations produced by octanoic acid, which is widely used in perfumes and disinfectants. Treating HepG2 cells with 0.39 μM octanoic acid increased p53 nuclear localization (3-fold) and stress kinase activity (2-fold) at 24 h. By 72 h p53 activity recovered close to baseline levels, but stress kinase activity was still elevated (1.4-fold). At a higher treatment concentration, 1.56 μM, octanoic acid decreased mitochondrial membrane potential (0.2-fold) at 24h but mitochondrial membrane potential recovered to background levels by 72 h. Since octanoic acid is a medium chain fatty acid, we speculate its effects on oxidative stress and mitochondrial function may be due to an increase in fatty acid metabolism (Gyamfi et al. 2012).

The next row of heatmaps in Figure 2(b) show the dynamic effects of dimethyl terephthalate (DMT), which is used in the production of polyesters. DMT produced a time-dependent increase (1.5-fold at 24 h and 2.5-fold at 72 h) in mitochondrial membrane potential and a minor decrease (0.7-fold at 24h and 0.7-fold and 72 h) in nuclear size at 0.39 μM. At 100 μM treatment

concentration, DMT caused a decrease in mitochondrial membrane potential (0.9-fold at 24 h and 0.3-fold at 72 h). The dual effects of DMT on MMP, increased at 0.39 μM but decreased at 100 μM, could be explained by transient mitochondrial hyperpolarization preceding apoptosis (Sánchez-Alcázar et al. 2000). The proportion of cells undergoing apoptosis was small, however, as there was no substantial decrease in cell number. As such, DMT exposure alters mitochondrial membrane potential with hyperpolarization at low concentrations and concentration-dependent transition to depolarization at a higher concentrations. The complex mechanisms underlying such a dose-dependent transition were difficult to interpret using these HCI data alone.

The organophosphate insecticide, chlorpyrifos-methyl (Figure 2(c)), caused microtubule disruption (0.2-fold change) at 1 h after 0.39 μM treatments, and a decrease (0.7-fold) in cell number after 72 h for a 200 μM (data not shown). Low concentrations of chlorpyrifos, which is structurally related to chlorpyrifos-methyl, in the 1-10 μM range, are known to disrupt the cytoskeleton in neurons (Flaskos et al. 2011). Chlorpyrifos is a known acetlycholinesterase inhibitor but the relevance to cytoskeletal disruption is unclear. Unlike octanoic acid, DMT and chlorpyrifos-methyl, butachlor (Figure 2(d)) produced concentration- and time-dependent perturbations across multiple endpoints. For a treatment concentration of 0.39 μM, butachlor increased p53 activity at 1 h (1.5-fold) and 24 h (2.5-fold), but p53 activity recovered to background levels by 72 h. This temporal trend of early p53 activation followed by later recovery was observed for increasing butachlor concentrations up to 6.25 μM. This recovery was not evident for butachlor concentrations above 6.25 μM; hence, the p53 response was more persistent at higher concentrations. The temporal trends in mitochondrial mass tracked along with p53 activity for this compound. Butachlor decreased cell number beyond 24 h at

concentrations above 100 μM. This widely used herbicide has been shown to induce DNA-damage and mitochondrial dysfunction in peripheral blood mononuclear (PBMN) cells (Dwivedi et al. 2012).

Dicofol, an organochlorine pesticide, invoked concentration-dependent early (1 and 24 h) perturbations in mitochondrial membrane potential, p53 activity, and stress kinase. At later time points (24 and 72 h), perturbations were observed in mitochondrial mass, cell cycle arrest, nuclear size and cell number (Figure 2(e)). Oxadiazon (bensulide), another organophosphate herbicide, also produced complex time- and concentration-dependent changes across all endpoints (Figure 2(f)).

Cell state trajectories

We used the concept of a system trajectory to analyze the concentration- and time-dependent stress responses produced by each chemical. A trajectory describes the dynamic changes in the state of HepG2 cells in response to chemical exposure. To interpret the HCI data in terms of cell state trajectories, we first assumed that the state of the HepG2 system could be defined by oxidative stress, stress kinase activity, mitochondrial function, cytoskeletal stability, cell cycle progression and cell number (which were all measured by HCI). Next, we assumed that the HCI data at each time point captures a snapshot of the state of the HepG2 system as it follows a chemical-induced trajectory. The heatmaps in Figure 2(a), for example, visualize trajectories for different treatment concentrations of octanoic acid. The rows of each heatmap (from bottom to top) correspond to discrete snapshots of the system perturbation at successive time points (0, 1, 24 and 72 h), and the columns of each heatmap show the system state based on 10 HCI

endpoints. We assume that the system is initially in a 'ground state' that defines the normal pattern so, by this definition there are no perturbations at 0 h.

Comparing the trajectories produced by different chemicals in Figure 2 revealed qualitative differences across concentrations and time points. For example, the trajectories produced by 0.39 μM and 1.56 μM octanoic acid show transitory perturbations in p53 and stress kinase activities at low concentrations, but not at high concentrations (Figure 2a). In contrast, butachlor produced quite clearly different trajectories in temporal response profiles at concentrations below 6.25 μM versus above 6.25 μM (Figure 2d). To enable quantitative analysis of trajectories both chemical-wise and concentration-wise, we developed an aggregate measure of overall system perturbation. The resulting perturbation vector (denoted as, $\vec{X}$) describes the changes in each endpoint at a given time, and the scalar magnitude of $\vec{X}$ (denoted as, X) measures the overall perturbation of the system by combining the contribution of individual endpoints. When the system is at the ground state, then scalar perturbation is essentially zero ($X = 0$), but as the cellular endpoints change due to chemical treatment the scalar perturbation increases ($X>0$).

Trajectories and system recovery

The scalar perturbations for the trajectories were calculated for the 967 chemicals and 10 treatment concentrations to investigate concentration- and time-dependent trends. The trends for 16 representative chemicals including, captan, dicofol, butachlor, dimethyl terephthalate, sodium L-ascorbate, octanoic acid, chlorpyrifos-methyl, oxadiazon, pioglitazone, farglitazaar, troglitazone, thiram, fludioxonil, mercuric chloride, fluazinam and tetramethrin are visualized in Figure 3. The ordinate and abscissa of each graph in Figure 3 shows the scalar perturbation (X)

and treatment duration (hours), respectively, for each of the 16 chemicals. The treatment concentrations for each chemical are visualized as colors from low (blue) to high (red). For example, trajectories elicited by butachlor treatments showed two different temporal trends in *X*. First, treatments less than 25 μM produced an early (1 and 24 h) increase in *X* that was followed by a later decrease (72 h). Second, trajectories elicited by butachlor treatments 25 μM and greater showed only an increase in *X* with time. We interpret these temporal trends as the integrated effect of chemical-induced stress, which causes *X* to deviate from the ground state, and adaptive cellular processes, which enable the system to recover to the ground state (Supplemental Material, Figure S1(c)). Thus, butachlor treatments less than 25 μM induced stress that dissipated with time because adaptive processes were activated in HepG2 cells that enabled system recovery. On the other hand, butachlor treatments 25 μM and above showed a monotonic increase with time, suggesting these higher concentrations overwhelmed the adaptive processes in HepG2 cells and consequently, the system could not recover to its ground state.

An adaptive recovery trend was also observed for octanoic acid, captan and dicofol (the results for other chemicals are not shown for brevity but are available as Supplemental Material, Excel Table S3). The dynamic capacity of HepG2 cells to recover varied by chemical and by concentration as illustrated by the cellular response to butachlor. Octanoic acid, on the other hand, produced smaller perturbations than butachlor and all trajectories implied system recovery. Of the 16 representative chemicals shown in Figure 3, partial or complete recovery trajectories were evident for some compounds. The two thiazoladinediones (pioglitazone and troglitazone) also displayed similar trends but it was difficult to compare differences quantitatively.

System tipping points

Visual inspection was useful for comparing the trends produced by different chemicals but not for quantifying concentration-dependent differences in perturbation and recovery. To further analyze the trends for each chemical, the rate of change of the scalar perturbation was calculated for the trajectories. The rate of change of the scalar perturbation across time (denoted as $V = \partial X/\partial t$) measures the "velocity" of the system perturbation at any given point in the trajectory (described further in Methods). The velocity is negative ($V<0$) when the system is on a trajectory that is recovering to the ground state. If the velocity is positive ($V>0$), then the system is on a trajectory that is not recovering. The system velocity for the trajectories was thus calculated using data for X at 24 and 72 h produced by all 967 chemicals and 10 treatment concentrations (results not shown). Trends in system velocity summarize the behavior of system trajectories and reveal concentration-dependent transitions that define the 'tipping points' for recovery of the HepG2 cellular system. We hypothesized the broader existence of such tipping points after studying the trajectories of chemicals such as, captan, dicofol and butachlor.

To mathematically identify tipping points of the HepG2 system using trajectories, the relationship between perturbation velocity (V) and concentration (c) was analyzed. We used the rate of change of V with respect to concentration (denoted as, $\partial_c V$) to identify the concentration threshold for system recovery (see Methods). Like velocity, $\partial_c V$ can have three possible values: (1) $\partial_c V<0$ for concentrations that produce recovery, (2) $\partial_c V>0$ for concentrations that do not produce recovery, and (3) $\partial_c V=0$ signifies the critical concentration and (denoted as, C_{cr}) corresponding to the tipping point of the system. The $\partial_c V$ and C_{cr} for 967 chemicals were calculated using the data at 24 and 72 h. We also conducted an uncertainty analysis for each

chemical to evaluate confidence in trajectories and to estimate variability in C_{cr} due to experimental noise (additional details are provided in Methods).

The scalar perturbation (X), velocity (V), derivative of velocity with respect to concentration ($\partial_c V$) for select chemicals at 72 h are shown in Figure 4. Two main concentration-dependent trends were used to determine the resilience of the HepG2 system to each chemical treatment. First, a subset of chemicals produced an overall decrease in $\partial_c V$ with increasing concentrations. This trend in $\partial_c V$ implied a recovering trajectory as invoked by, for example DMT, sodium L-ascorbate, octanoic acid, chlorpyrifos-methyl, fludioxonil and tetramethrin. Second, a subset of chemicals elicited an overall increase in $\partial_c V$ with increasing treatment concentrations. This implied a non-recovering trajectory that contained tipping points in the cellular system identified by the condition, $\partial_c V=0$. Based on our analysis, butachlor, oxadiazon, pioglitazone, farglitazar, troglitazone, and thiram had critical concentrations of 2.6 ± 0.5 μM, 17.6 ± 1.2 μM, 28.4 ± 5.0 μM, 17.0 ± 2.4 μM, 4.5 ± 2.6 μM, and 69.1 ± 5.7 μM, respectively.

The resilience analysis of the HepG2 system trajectories showed that roughly a third (334/967) of all chemicals produced recovery, another third (336/967) did not result in recovery and the remainder (297/967) did not produce trajectories with substantial perturbations, or sufficient confidence to place them in either category. Captan, mercuric chloride and fluazinam are examples of chemicals that produced trajectories with low confidence. Visual inspection of trajectories for these chemicals showed complex concentration-dependent trends in $\partial_c V$ (see Figure 4). Overall, 104 chemicals produced complex trends in $\partial_c V$ and a majority (71/104) produced trajectories with low confidence. Complex trends in $\partial_c V$ could be indicative of noise and may require additional experimental data for improving confidence in the results.

We selected the 336 chemicals that elicited tipping points in the HepG2 system to compare critical concentrations with lowest effect concentrations (LEC) and the results are visualized in Figure 5. Out of 336 chemicals that produced tipping points, only 124 had an LEC across any of the 10 endpoints at 72 h. On average, the critical concentration (C_{cr}) was 13 times lower than the lowest LEC for 86% (106/124) of the chemicals, whereas the LEC was 6 times lower than the C_{cr} for 15% (18/124) of the chemicals. The C_{cr} was generally between 5 and 15 times (25^{th} and 75^{th} percentiles, respectively) lower than the lowest LEC. The results of the resilience analysis for 967 chemicals, along with critical points, are given in Supplemental Material, Excel Table S3.

Discussion

From these results we conclude that HCI can be used to identify *in vitro* cellular tipping points in response to chemical-induced perturbations. Application of HCI for screening has been used previously to study the effects of chemicals on cellular systems (O'Brien et al. 2006; Abraham et al. 2008), and to profile molecular changes underlying cellular processes (Neumann et al 2010; Held et al 2010). Here we analyzed time-course HCI data to investigate the dynamic response of the HepG2 cells to 10 concentrations of 967 chemicals. The time-dependent perturbations of HepG2 cells were analyzed as state trajectories that describe the sequential perturbations in the system state as it adapts to chemical exposure. A novel computational approach was developed to analyze trajectories by quantifying the dynamic response of the system across all chemical treatments. The quantity of the scalar perturbation was termed the "velocity" because it measures the rate at which the aggregate system state deviates away from, or returns to, the normal state. We hypothesize that this velocity is a measure of system resilience, and it can be

used to identify a dose-dependent transition in system recovery. We call this dose-dependent transition a 'tipping point' and believe it can be used as a point of departure in a high-throughput risk assessment context (Judson et al. 2011).

Current toxicological tests are based on identifying apical adverse effects to define a point of departure for risk assessment. Adversity has been traditionally defined as a "biochemical, morphological or physiological change (in response to a stimulus) that either singly or in combination adversely affects the performance of the whole organism or reduces the organism's ability to respond to an additional environmental challenge" (Lewis et al. 2002). Characterizing adverse effects using high-throughput assays is a key problem for 21st Century Toxicology (Keller et al. 2012). HCI can measure adaptive cell stress responses, albeit in a cell-autonomous context (Simmons et al. 2009). An adaptive response is a homeostatic process that is activated by the system to survive in a new environment without impairment of function (Keller et al. 2012). We believe that our analysis of trajectories and tipping points brings us a step closer to realizing the vision of 21st Century Toxicology by providing a framework to identify where "transition points occur between adaptive changes and adverse effects" (Keller et al. 2012). However, implementing this vision will require much more work on interpreting the role of cell-autonomous adaptive responses in the context of pathways that lead to *in vivo* adverse outcomes (Boekelheide and Andersen 2010).

Biological systems have evolved adaptive mechanisms that allow them to maintain a constant internal environment despite variation in external conditions (Kitano 2004). A number of homeostatic control systems compensate for chemical-induced perturbations in cells. Cells possess diverse signaling pathways to sense state changes due to reactive oxygen species (ROS),

DNA adducts, protein denaturation, glutathione depletion, etc. and can activate feedback control processes, usually via genetic regulatory networks, to maintain their internal state (Simmons et al. 2009). As the concentration of a chemical rises and the intracellular state becomes increasingly perturbed, different feedback control mechanisms are incrementally activated and, potentially overwhelmed. The complexity of these interconnected processes could explain why we observed dose-dependent transitions in the recovery of HepG2 cells. Dose-dependent transitions have been described in the mechanisms of toxicity for a number of chemicals (Slikker et al. 2004), but such effects have not been studied systematically for *in vitro* systems. Zhang et al. (2008) have proposed a control-theoretic approach to model the action of anti-stress genetic regulatory networks in maintaining cell state, and to further explain the observation of dose-dependent transitions in biological responses. Experimental evidence (Slikker et al. 2004), together with mathematical models (Zhang et al. 2008), support the notion that there are dose-dependent transitions in some biological responses; however, identifying *in vivo* thresholds for toxicity is expected to be multifactorial (time and concentration-dependent) and, thus, is extremely challenging.

Assessing the global state of a cellular system, which is defined by thousands of biological molecules, is a challenging problem but a relatively small number of pathways may be involved in responding to chemical-induced stress. A set of such stress response pathways proposed by Simmons et al. (2009) includes: oxidative stress, heat shock response, DNA damage response, hypoxia, ER stress, metal stress, inflammation, and osmotic stress. Our study included a subset of these stress responses but we also considered mitochondrial, cytoskeletal, and cell cycle changes, which are relevant measures of cell health. There is also growing evidence for cross-

talk between stress response pathways, which enhances the adaptive response of cells to environmental stressors (Simmons et al. 2009). Assuming a finite number of stress response pathways, the amplification of stress responses by cross-talk, and considering the sensitivity of HCI, we believe our study reasonably assessed adaptation of HepG2 cells to 967 chemicals. In future work we plan to extend our analysis to include additional stress response pathways.

It is important to note that our results may be limited by the small number of time points used in this study. As our analysis combined HCI data from two independent experiments (ToxCast Phase I (Judson et al. 2010) and Phase II), the 1 h time point was only collected for a subset of 308/967 chemicals, primarily due to cost considerations, and preliminary results indicating that the 1 h time point was helpful for visualizing trajectories, but not essential to the analysis and conclusions. The analysis of tipping points is based on the complete set of observations for all 967 chemicals at 24 and 72 h. We recognize that a more fine-grained temporal resolution or additional time points may produce different results. In particular, some chemicals that produced time-dependent results, but did not display recovery at 72 h, may exhibit recovery at later time points. We hope to evaluate the impact of additional time points on the analysis of trajectories and tipping points in future work.

Another potential limitation is the cell system used in this study. The HepG2 cells are an immortalized line with characteristics that differ from normal hepatocytes. For example, these cells easily proliferate in culture but have limited metabolic activity compared to primary hepatocytes (O'Brien et al. 2006; Abraham et al. 2008). The HepG2 cell model used in this study was a two-dimensional monoculture that does not reflect the complex cell-to-cell interactions present in intact organs that have multiple cell types. So, it is quite possible that the trajectories

produced by chemicals in this cell-autonomous model will be different from those in more complex cell-based systems. However, we fully expect that the general categories of observations and the quantitative approach developed in the present study will be transferable to other cellular systems.

Tipping-points for chemical-induced toxicity are not a new concept; however, defining them theoretically and identifying them experimentally is challenging. Chemical-induced toxicity is believed to occur when adaptive pathways in biological systems are overwhelmed, and usually when the stressor causes perturbations that are sufficiently large (Krewski et al. 2010). The idea that biological systems have a homeostatic capacity implies the existence of tipping points. If biological tipping points could be quantified for a chemical, they could be used to estimate levels of chemical exposure that overwhelm this homeostatic capacity. We believe that our approach for analyzing tipping points of cellular systems is an initial step toward quantifying *in vitro* regions of safety for chemicals. In combination with sophisticated methods for quantitative *in vitro* to *in vivo* extrapolation (Wetmore 2014), cellular tipping points could be used as a point of departure for high-throughput risk assessment. This will require additional evaluation of our approach using more chemicals, cell-based models, time points and endpoints.

Conclusions

Our findings demonstrate the potential utility of time-course high-throughput, high-content biological assays for elucidating cellular phenotypic behaviors of chemicals and identifying tipping points of cellular systems. The number of chemicals used in this study, and range of cellular end points measured, suggest that this analysis approach can be utilized to provide valuable information about the effects of new chemicals and critical concentrations where the

cell responses fail to return to control levels. Our findings also underscore the importance of considering the temporal evolution of biological systems as a means of resolving adaptive changes that either lead to recovery or progress to cellular injury.

References

Abraham VC, Towne DL, Waring JF, Warrior U, Burns DJ. 2008. Application of a high-content multiparameter cytotoxicity assay to prioritize compounds based on toxicity potential in humans. J Biomol Screen 13:527–537; doi:10.1177/1087057108318428.

Attene-Ramos MS, Miller N, Huang R, Michael S, Itkin M, Kavlock RJ, et al. 2013. The Tox21 robotic platform for the assessment of environmental chemicals - from vision to reality. Drug Discov. Today 18:716–723; doi:10.1016/j.drudis.2013.05.015.

Blackman RB, Tukey JW. 1958. *The Measurement of Power Spectra from the Point of View of Communications Engineering*. Dover Publications, Inc. New York.

Boekelheide K, Andersen ME. 2010. A mechanistic redefinition of adverse effects - a key step in the toxicity testing paradigm shift. ALTEX 27: 243–252.

Cellomics 2007a. Cell Cycle BioApplication Guide. Cellomics, Inc., 100 Technology Drive Pittsburgh, Pennsylvania 15219.

Cellomics 2007b. Compartmental Analysis BioApplication Guide. Cellomics, Inc., 100 Technology Drive Pittsburgh, Pennsylvania 15219.

Dwivedi S, Saquib Q, Al-Khedhairy AA, Musarrat J. 2012. Butachlor induced dissipation of mitochondrial membrane potential, oxidative DNA damage and necrosis in human peripheral blood mononuclear cells. Toxicology 302:77–87; doi:10.1016/j.tox.2012.07.014.

Flaskos J, Nikolaidis E, Harris W, Sachana M, Hargreaves AJ. 2011. Effects of sub-lethal neurite outgrowth inhibitory concentrations of chlorpyrifos oxon on cytoskeletal proteins and acetylcholinesterase in differentiating N2a cells. Toxicol. Appl. Pharmacol. 256:330–336; doi:10.1016/j.taap.2011.06.002.

Giuliano KA, Johnston PA, Gough A, Taylor DL. 2006. Systems cell biology based on high-content screening. Meth. Enzymol. 414:601–619; doi:10.1016/S0076-6879(06)14031-8.

Gyamfi D, Everitt HE, Tewfik I, Clemens DL, Patel VB. 2012. Hepatic mitochondrial dysfunction induced by fatty acids and ethanol. Free Radic. Biol. Med.; doi:10.1016/j.freeradbiomed.2012.09.024.

Held M, Schmitz MHA, Fischer B, Walter T, Neumann B, Olma MH, et al. 2010. CellCognition: time-resolved phenotype annotation in high-throughput live cell imaging. Nat. Methods 7:747–754; doi:10.1038/nmeth.1486.

Judson R, Richard A, Dix DJ, Houck K, Martin M, Kavlock R, et al. 2009. The toxicity data landscape for environmental chemicals. Environ. Health Perspect. 117:685–695; doi:10.1289/ehp.0800168.

Judson RS, Houck KA, Kavlock RJ, Knudsen TB, Martin MT, Mortensen HM, et al. 2010. In vitro screening of environmental chemicals for targeted testing prioritization: The toxcast project. Environmental Health Perspectives 118:485-492.

Judson RS, Kavlock RJ, Setzer RW, Hubal EAC, Martin MT, Knudsen TB, et al. 2011. Estimating toxicity-related biological pathway altering doses for high-throughput chemical risk assessment. Chem. Res. Toxicol. 24:451–462; doi:10.1021/tx100428e.

Kavlock RJ, Austin CP, Tice RR. 2009. Toxicity testing in the 21st century: implications for human health risk assessment. Risk Anal. 29:485–487; discussion 492–497; doi:10.1111/j.1539-6924.2008.01168.x.

Kavlock R, Chandler K, Houck K, Hunter S, Judson R, Kleinstreuer N, et al. 2012. Update on EPA's ToxCast program: providing high throughput decision support tools for chemical risk management. Chem. Res. Toxicol. 25:1287–1302; doi:10.1021/tx3000939.

Keller DA, Juberg DR, Catlin N, Farland WH, Hess FG, Wolf DC, et al. 2012. Identification and characterization of adverse effects in 21st century toxicology. Toxicol. Sci. 126:291–297; doi:10.1093/toxsci/kfr350.

Kitano H. 2004. Biological robustness. Nat. Rev. Genet. 5:826–837; doi:10.1038/nrg1471.

Krewski D, Acosta D Jr, Andersen M, Anderson H, Bailar JC 3rd, Boekelheide K, et al. 2010. Toxicity testing in the 21st century: a vision and a strategy. J Toxicol Environ Health B Crit Rev 13:51–138; doi:10.1080/10937404.2010.483176.

Lewis, Richard W., Richard Billington, Eric Debryune, Armin Gamer, B. Lang, and Francis Carpanini. 2002. "Recognition of Adverse and Nonadverse Effects in Toxicity Studies." Toxicologic Pathology 30 (1): 66–74.

National Research Council (NRC). 2007. *Toxicity Testing in the 21st Century: A Vision and a Strategy*. Committee on Toxicity Testing and Assessment of Environmental Agents. The National Academies Press, Washington, D.C.

Neumann B, Walter T, Hériché J-K, Bulkescher J, Erfle H, Conrad C, et al. 2010. Phenotypic profiling of the human genome by time-lapse microscopy reveals cell division genes. Nature 464:721–727; doi:10.1038/nature08869.

O'Brien PJ, Irwin W, Diaz D, Howard-Cofield E, Krejsa CM, Slaughter MR, et al. 2006. High concordance of drug-induced human hepatotoxicity with in vitro cytotoxicity measured in a novel cell-based model using high content screening. Arch. Toxicol. 80:580–604; doi:10.1007/s00204-006-0091-3.

Python. 2014. Available: https://www.python.org/ [accessed 1 August 2014].

Sánchez-Alcázar JA, Ault JG, Khodjakov A, Schneider E. 2000. Increased mitochondrial cytochrome c levels and mitochondrial hyperpolarization precede camptothecin-induced apoptosis in Jurkat cells. Cell Death Differ. 7:1090–1100; doi:10.1038/sj.cdd.4400740.

Simmons SO, Fan C-Y, Ramabhadran R. 2009. Cellular stress response pathway system as a sentinel ensemble in toxicological screening. Toxicol. Sci. 111:202–225; doi:10.1093/toxsci/kfp140.

Slikker W Jr, Andersen ME, Bogdanffy MS, Bus JS, Cohen SD, Conolly RB, et al. 2004. Dose-dependent transitions in mechanisms of toxicity: case studies. Toxicol. Appl. Pharmacol. 201:226–294; doi:10.1016/j.taap.2004.06.027.

U.S. EPA (Environmental Protection Agency). 2014. ToxCast Phase I and Phase II chemicals. Available: http://www.epa.gov/comptox/toxcast/chemicals.html [accessed 21 September 2015].

Wetmore BA. 2014. Quantitative in vitro-to-in vivo extrapolation in a high-throughput environment. Toxicology; doi:10.1016/j.tox.2014.05.012.

Zhang Q, Pi J, Woods CG, Jarabek AM, Clewell HJ 3rd, Andersen ME. 2008. Hormesis and adaptive cellular control systems. Dose Response 6:196–208; doi:10.2203/dose-response.07-028.Zhang.

Figure Legends

Figure 1. Hypothetical dynamic system perturbations as trajectories and calculation of tipping points. (a) The green curve depicts a hypothetical trajectory across observations at time t (X^t) shown on the basis of two endpoints (x_i and x_j). (b) The perturbation velocity (V) is calculated as the derivative of the scalar perturbation ($|X|$) with respect to time (shown in green). (c) Three different types of trajectories are shown using $|X|$: trajectories that describe the normal behavior of the system (shown in green); adaptive trajectories, which include some perturbation of the system state followed by recovery (shown in orange); and adverse trajectories that show initial adaptive responses followed by lack of recovery at later times (shown in red). (d) The relationship between the velocity, concentration and time is given by a continuous surface, $V = f(c,t)$. (e) The rate of change of velocity with respect to concentration is given by: $\partial_c V = \partial V/\partial c = \partial^2 X/\partial t \partial c$. (f) Solving $\partial_c V = 0$ gives the critical concentration, (C_{cr}).

Figure 2. Concentration and time dependent perturbations produced by chemicals. From top to bottom each row of heatmaps shows the perturbations produced by increasing concentrations of: (a) octanoic acid, (b) dimethyl terephthalate, (c) chlorpyrifos-methyl, (d) butachlor, (e) dicofol, and (f) oxadiazon. Each heatmap shows the endpoints (columns), time in hours (rows) and perturbations (colors) produced by each concentration (title). The endpoints include p53 activity, stress kinase (SK), oxidative stress (OS), microtubules (Mt), mitochondrial mass (MM), mitochondrial membrane, potential (MMP), mitotic arrest (MA), cell cycle arrest (CCA), nuclear size (NS) and cell number (CN). The colors signify no effect (yellow), increase (red), and decrease (blue), where magnitude of changes are shown in the color bar on the right.

Figure 3. Magnitude of perturbations for trajectories produced by fixed treatment concentrations of different chemicals. Each graph shows scalar perturbations (y-axis) across time (x-axis) for multiple doses of a chemical. The colors signify treatment concentrations ranging from low (blue) to high (red).

Figure 4. Trajectory analysis and critical concentrations of different chemicals at 72h. The y-axis of each graph shows the scalar system perturbation (X = green), velocity (V = blue) and

derivative of velocity with respect to concentration ($\partial_c V$ = red), and uncertainty analysis of $\partial_c V$ (light red). The x-axis of each graph shows the treatment concentration of the chemical (μM). Dimethyl terephthalate, sodium L-ascorbate, octanoic acid, chlorpyrfos-methyl, fludioxonil and tetramethrin produced trends in $\partial_c V$ consistent with system recovery. Butachlor, oxadiazon, pioglitazone, farglitazar, troglitazone, and thiram elicit trajectories with tipping points. Captan, mercuric chloride and fluazinam produced complex trends in $\partial_c V$ that could be indicative of experimental noise.

Figure 5. Critical concentrations (C_{cr}) for 340 chemicals at 72h. Chemicals are sorted by C_{cr} in descending order from top to bottom (y-axis) and each row shows the C_{cr}, lowest effect concentration (LEC), scalar perturbation ($|X|$), and velocity *(V)*. (a) C_{cr} (μM) is shown as a point along the x-axis with the uncertainty as grey line, minimum LEC as a green point, and select chemicals are labeled. (b) LEC (μM) across p53, SK (stress kinase), OS (oxidative stress), Mt (microtubules), MM (mitochondrial mass), mitochondrial membrane potential (MMP), mitotic arrest (MA), cell cycle arrest (CCA), nuclear size (NS), and cell number (CN). The LEC value is represented by: no effect (pink), and red saturation as shown in the colorbar on the right. (c) $|X|$ as a heatmap across concentrations (μM) where magnitude is represented by color saturation (values shown in colorbar on the right). (d) V as a heatmap across concentrations (μM) where $V>0$ (reds), $V<0$ (blues) and $V=0$ (white).

Environ Health Perspect DOI: 10.1289/ehp.1409029
Advance Publication: Not Copyedited

Figure 1

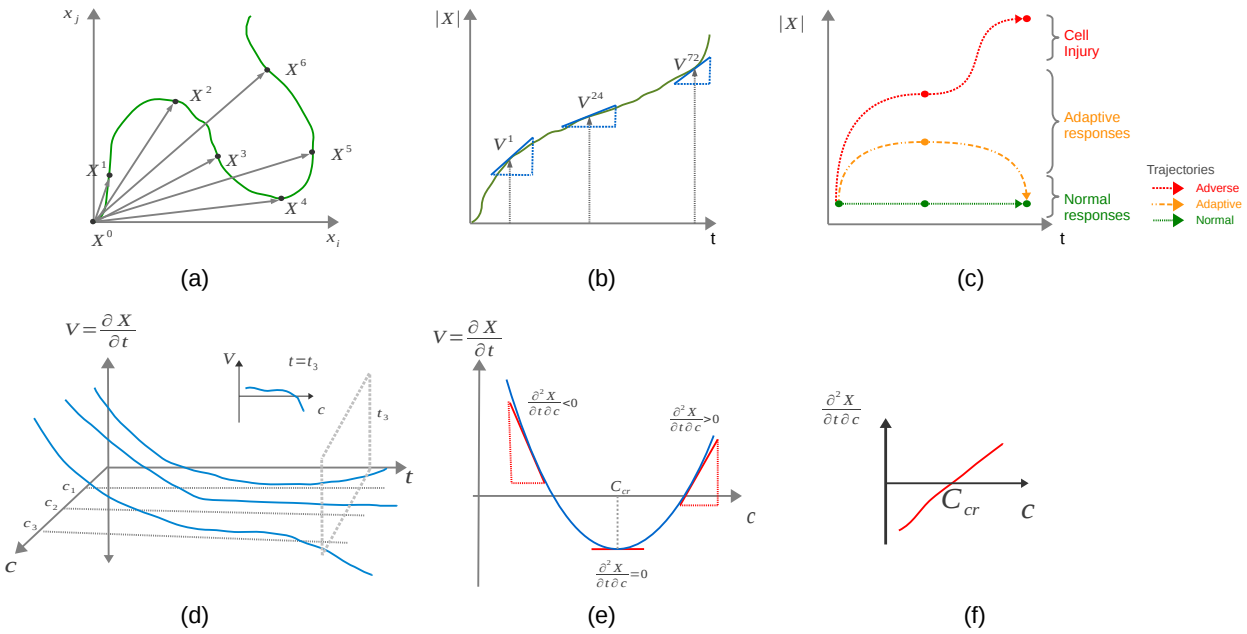

Environ Health Perspect DOI: 10.1289/ehp.1409029
Advance Publication: Not Copyedited

Figure 2

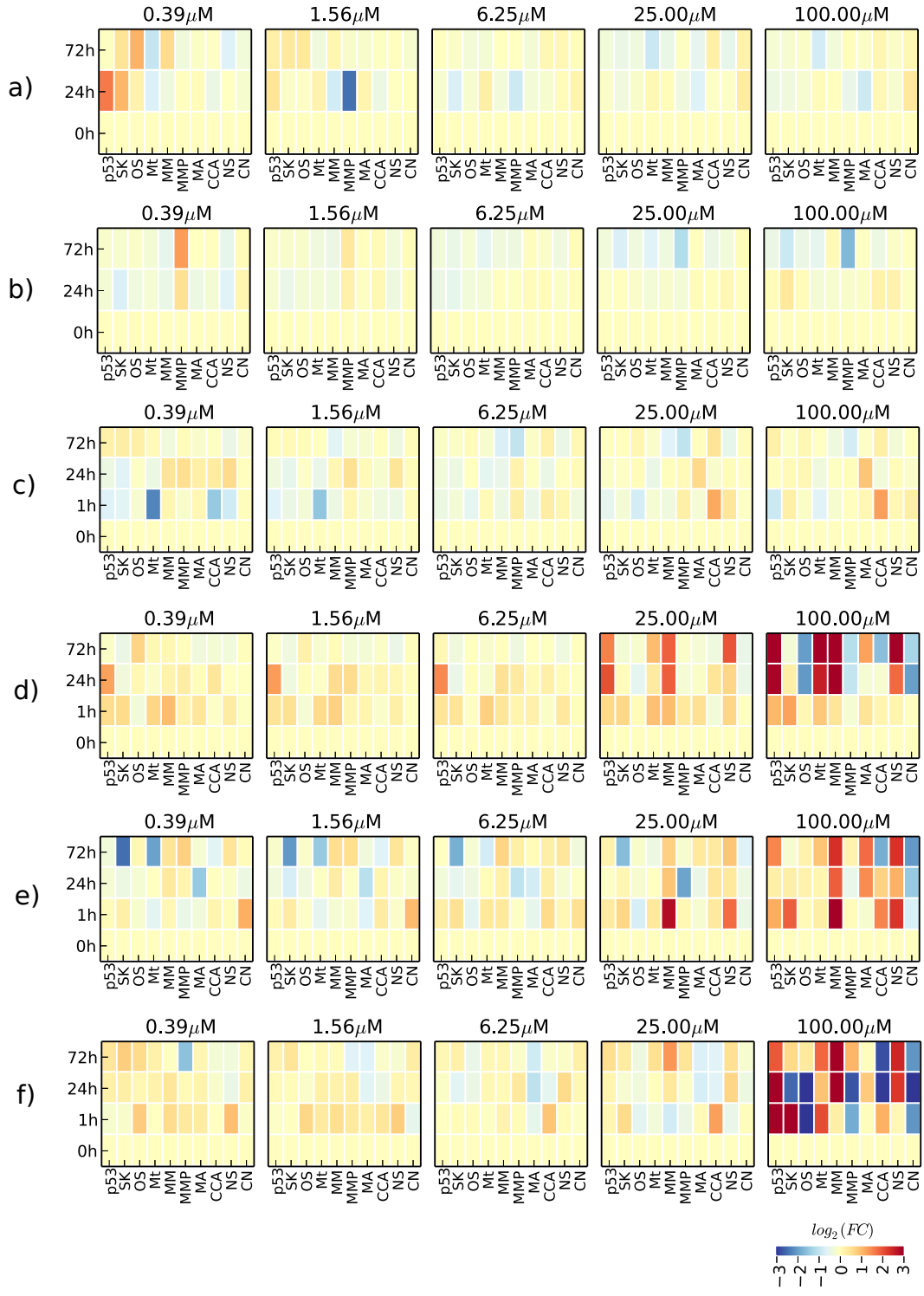

Figure 3

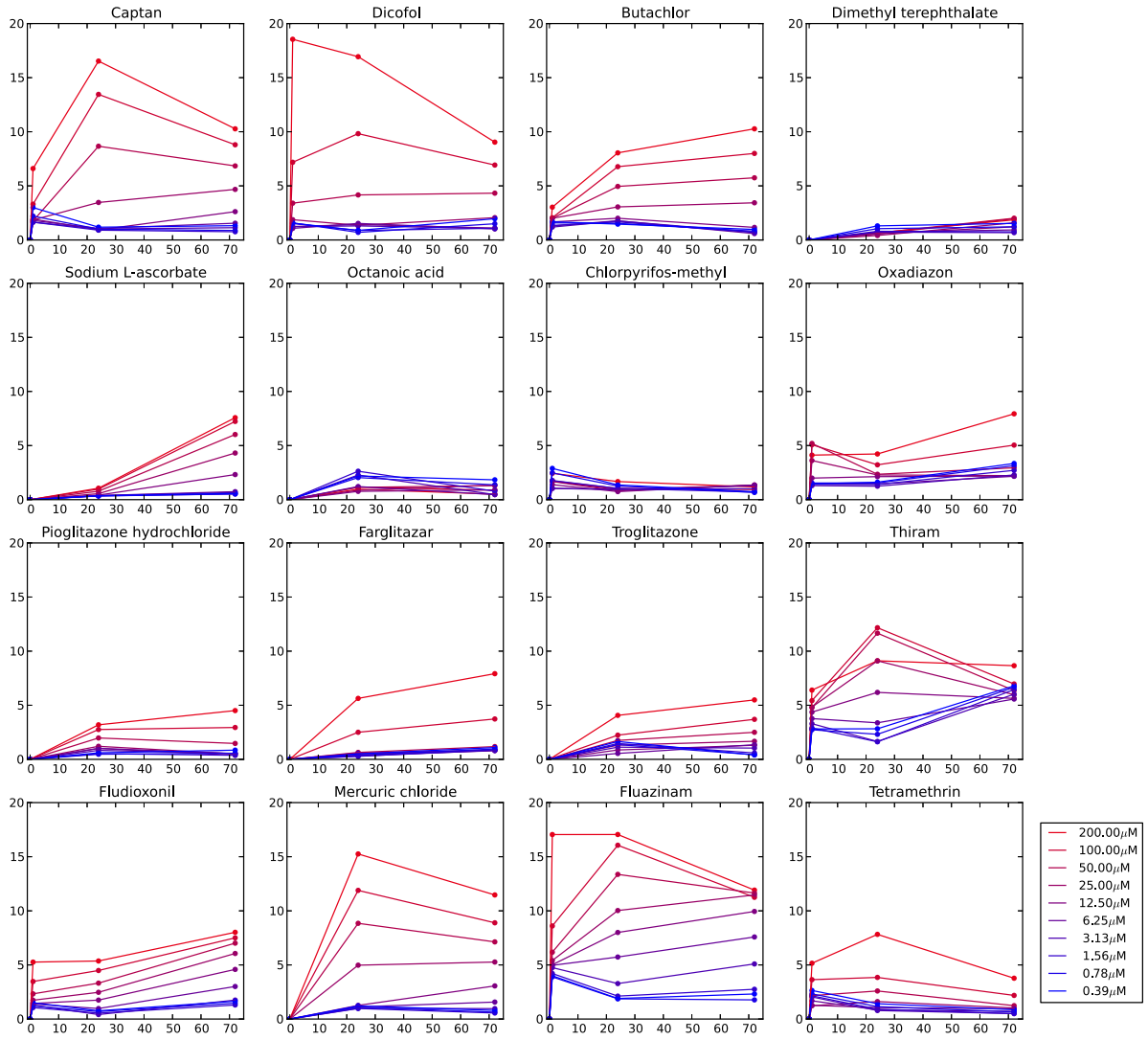
Captan
Dicofol
Butachlor
Dimethyl terephthalate
Sodium L-ascorbate
Octanoic acid
Chlorpyrifos-methyl
Oxadiazon
Pioglitazone hydrochloride
Farglitazar
Troglitazone
Thiram
Fludioxonil
Mercuric chloride
Fluazinam
Tetramethrin
200.00μM
100.00μM
50.00μM
25.00μM
12.50μM
6.25μM
3.13μM
1.56μM
0.78μM
0.39μM

Environ Health Perspect DOI: 10.1289/ehp.1409029
Advance Publication: Not Copyedited

Figure 4

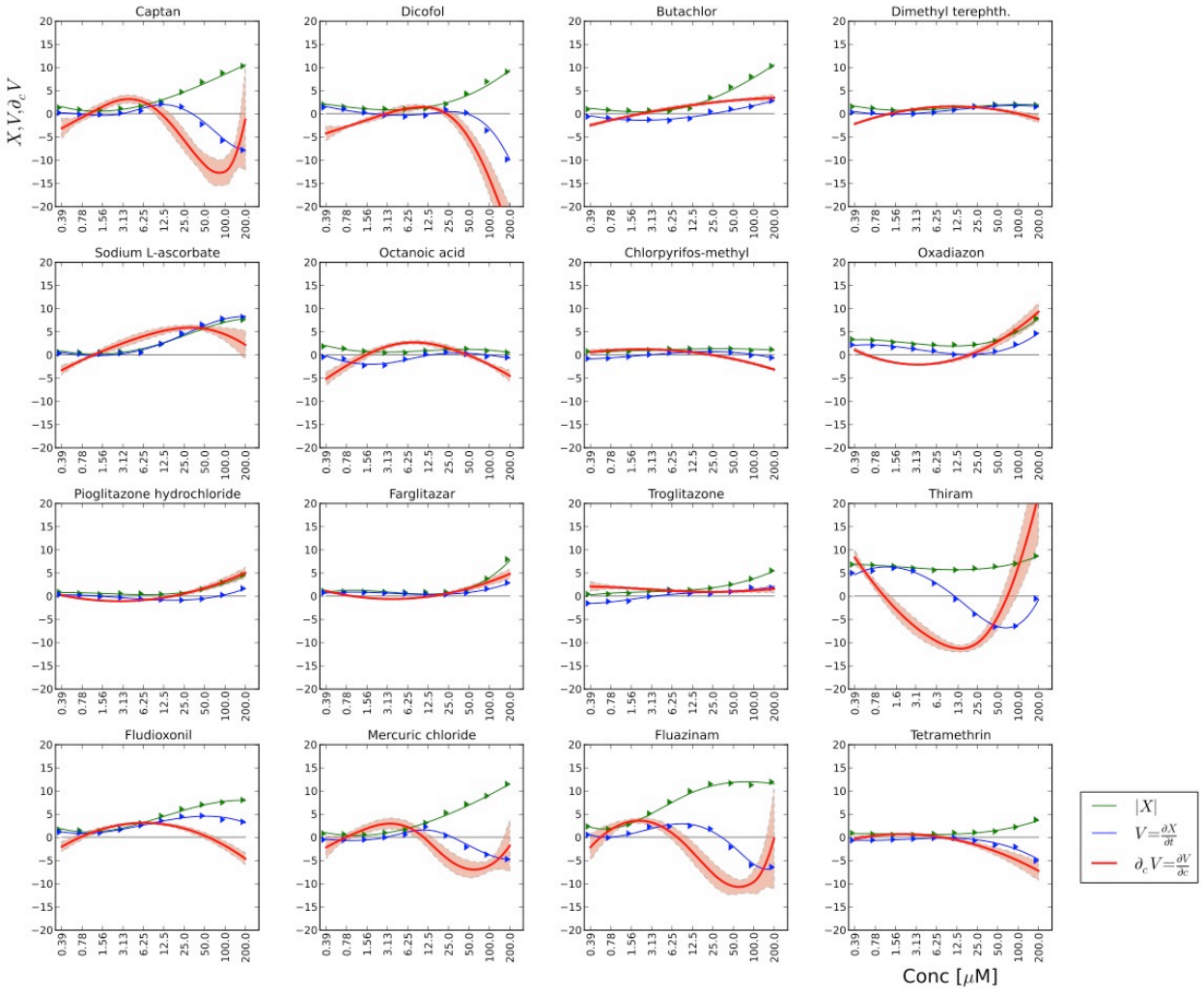

Figure 5.

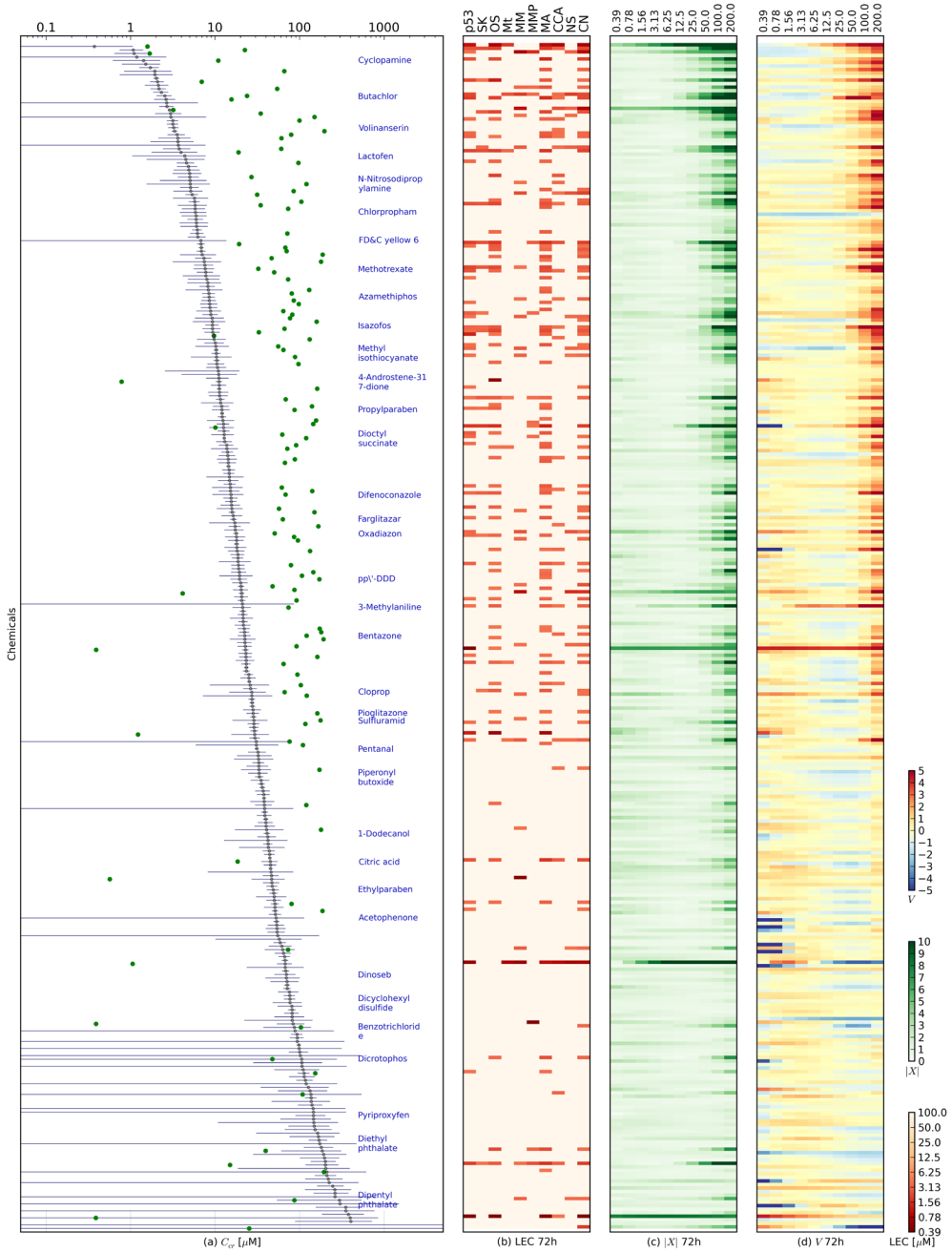
0.1
1
10
100
1000
Chemicals
Cyclopamine
Butachlor
Volinanserin
Lactofen
N-Nitrosodiprop ylamine
Chlorpropham
FD&C yellow 6
Methotrexate
Azamethiphos
Isazofos
Methyl isothiocyanate
4-Androstene-31 7-dione
Propylparaben
Dioctyl succinate
Difenoconazole
Farglitazar
Oxadiazon
ppÍ-DDD
3-Methylaniline
Bentazone
Cloprop
Pioglitazone
Sulfluramid
Pentanal
Piperonyl butoxide
1-Dodecanol
Citric acid
Ethylparaben
Acetophenone
Dinoseb
Dicyclohexyl disulfide
Benzotrichlorid e
Dicrotophos
Pyriproxyfen
Diethyl phthalate
Dipentyl phthalate
(a) C_{cy} [μM]
p53
SK
OS
Mt
MM
MMP
MA
CCA
NS
CN
(b) LEC 72h
0.39
0.78
1.56
3.13
6.25
12.5
25.0
50.0
100.0
200.0
(c) $|X|$ 72h
(d) V 72h
V
$|X|$
LEC [μM]